Segmentation and Measurement of Chronic Wounds for Bioprinting

Peyman Gholami, Mohammad Ali Ahmadi-pajouh, Nabiollah Abolftahi, Ghassan Hamarneh, *Senior Member, IEEE,* and, Mohammad Kayvanrad

Abstract

Objective: To provide a proof-of-concept tool for segmenting chronic wounds and transmitting the results as instructions and coordinates to a bioprinter robot and thus facilitate the treatment of chronic wounds.

Methods: Several segmentation methods used for measuring wound geometry, including edge-detection and morphological operations, region-growing, Livewire, active contours, and texture segmentation, were compared on 26 images from 15 subjects. Ground truth wound delineations were generated by a dermatologist. The wound coordinates were converted into G-Code understandable by the bioprinting robot. Due to its desirable properties, alginate hydrogel synthesized by dissolving 16% (w/v) sodium-alginate and 4% (w/v) gelatin in deionized water and used for cell encapsulation.

Results: Livewire achieved the best performance, with minimal user interaction: 97.08%, 99.68% 96.67%, 96.22, 98.15, and 32.26, mean values, respectively, for accuracy, sensitivity, specificity, Jaccard Index, Dice Similarity Coefficient, and Hausdorff Distance. The bioprinter robot was able to print skin cells on the surface of skin with a 95.56% similarity between the bioprinted patch's dimensions and the desired wound geometry.

Conclusion: We have designed a novel approach for the healing of chronic wounds, based on semi-automatic segmentation of wound images, improving clinicians' control of the bioprinting process through more accurate coordinates.

Significance: This study is the first to perform wound bioprinting based on image segmentation. It also compares several segmentation methods used for this purpose to determine the best.

Index Terms— **bioprinting, chronic wound, image segmentation, Aliginate-gel, bio-ink.**

I. INTRODUCTION

CHRONIC wounds, with an approximate annual care cost of $50 billion and 2% prevalence in the general population of the United States, are a major challenge of today's skin pathology and dermatological science [1]. Many treatment approaches have been implemented, among which the traditional tissue-engineering-based treatments are increasingly common [2]. Such treatments usually involve fabrication of 3D-interconnected-pore networks, called scaffolds, which maintain the shape and mechanical properties of the desired structures for cell attachment, and supply cell-proliferation substrates, needed for the regeneration of 3D tissues. However, scaffold-based tissue, regardless of its benefits and various applications, can be plagued by limitations and problems, e.g., the lack of precision in cell placement, limited cell density, the need for organic solvents, insufficient interconnectivity, and the inability to control pore distribution and dimensions [2]. These common limitations necessitated the development of novel methods to improve the wound healing time and resulted in considering other methods. One brand-new method is treating chronic wounds using bioprinting based on desktop printers, which precisely place manufactured skin structures consisting of different kinds of cells or biomaterials on wounds in a controlled fashion.

To implement wound bioprinting, an accurate measurement of wound surface specifications is required. While contact measurement of wounds, e.g., ruler, wound tracing, and planimetry methods, are still widely used [3], these methods are generally slow, inaccurate, and often problematic [4]. Thus, these limitations along with the need for high-speed methods for measuring different soft materials such as human body tissues, including the skin, have led to the emergence of non-contact fast measurement methods.

Different non-contact wound and burn measurement methods, e.g., ultrasonic, optical, and image processing-based, are under development [5]. However, most of those currently being used require complicated hardware, high processing capabilities and complex arrangements, leading to high costs and low adjustability. Hence, image processing methods, which can be done using only a simple digital camera, are the most suitable and inexpensive option for many non-contact measurements. Fig. 1 represents typical non-contact and contact measurement methods. Our goal is to develop a low-cost, adjustable, and easy-to-use system for non-contact measurement of wound specifications on the skin surface and print the obtained geometries in an efficient way.
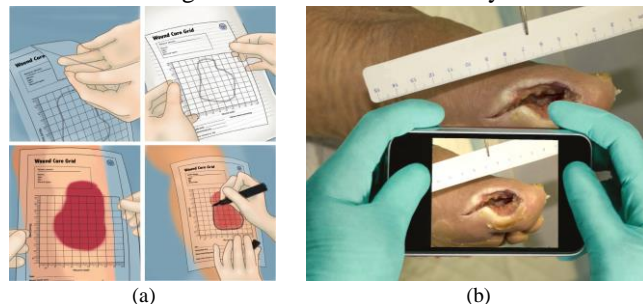
P. Gholami, is with the School of Optometry and Vision Science, Department of System Design Engineering at University of Waterloo, ON, Canada (e-mail: pgholami@uwaterloo.ca).

M. A. Amadi-Pajouh, N. Abolfathi and M. Kayvanrad are with the Biomedical Engineering Department at Amirkabir University of Technology, Tehran, Iran (e-mail: pajouh@aut.ac.ir; nabolfathi@aut.ac.ir; mkayvanrad@aut.ac.ir).

G. Hamarneh is with the School of Computing Science at Simon Fraser University, Burnaby, Canada (e-mail: hamarneh@sfu.ca).

| (a) | (b) |

Fig. 1. Measuring wounds using (a) a contact and (b) a non-contact method.

TABLE I
A REVIEW OF CURRENT STUDIES ON WOUND SEGMENTATION

Papers	Application	Segmentation Methodology	No. of Images	Imaging Conditions	Segmentation Results
Fauzi *et al.,* 2015[6]	WS, WM and characterization	RYKW map, Region-growing and Optimal thresholding	80	With background	75.1% accuracy
Wang *et al.,* 2015 [7]	WS and healing status	Mean-shift (boundaries) K-mean (color segmentation)	30 moulage, 34 real patients	with the assistance of an image capture box	Not available
Loizou *et al.,* 2013 [8,9]	Wound healing	Snake (segmentation), Texture feature (healing)	77 images, 11 subjects	Wound region only, polarized filter, dark room	Not available
Wannous *et al,* 2007-2011 [10-12]	WS	Mean shift, JSEG	25	With background, controlled conditions	73.3-80.2% (granulation tissue), 56.4-69.8% (slough tissue), 64.9-70.7% (necrosis tissue)
Hettiarachchi *et al.,* 2013 [13]	WS	AC	20	Wound region only, controlled conditions	90.0% accuracy
Veredas *et al.,* 2010 [14]	WS and tissue characterization	Mean shift and region growing	113	Wound region only, White background	78.7% sensitivity 94.7% specificity 91.5% accuracy
Hani *et al.,* 2012 [15]	WS	ICA and K-means	30	Wound region only	88.2% sensitivity 98.8% specificity
Perez *et al.,* 2001 [16]	WS and tissue analysis	Region growing and RGBSI analysis	Not available	Leg ulcers only	Not available
Wantanajittikul *et al.,* 2011 [17]	Burn segmentation, degree identification	FCM and Morphology, Texture analysis	5	Burn cases only	92% PPV, 84% sensitivity
Song and Sacan, 2012 [18]	WS, identification	Edge Detection, K-means clustering, Thresholding, Region Growing	92 images, 14 patients	Wound region manually traced	Not available
Kolesnik and Fexa, 2004-2006 [19,20]	WS, classification	SVM, Texture analysis, Deformable Snake	50	Camera surrounded by a ring of LED lights	Error rate of 6.56% (color), 22.16% (text.), 5.8% (color&text.)
Silveira *et al.,* 2009 [21]	Skin Melanoma segmentation	AT, GVF, AS, C-LS, EM-LS, FBSM	100	Corner and hair removal	12.63 Hammoude distance, 95.47% True detection rate, 36.90 Hausdorff distance,

II. RELATED WORKS

Several studies have addressed wound segmentation (WS) and wound measurement (WM) [6-21] using different image processing methods. Table I summarizes the most significant works in WS [6]. There are three main types of wound tissues: granulation, slough, and necrosis which are characterized in some papers [6,14,19,20]. Other works, on skin melanoma segmentation and cancer detection, are not mentioned in this table. Most studies are performed under controlled photography conditions, such as special backgrounds, or focusing only on specific wound regions or types, e.g., leg ulcers. There is no mention of wound geometry, which directly affects the bioprinting process because more-complex wounds with detailed edges require more accurate segmentation methods. Moreover, applications of most existing works are confined to only a few limited cases, such as tracking the healing process, which are insufficiently accurate and not applicable for bioprinting.

For moving and dispensing skin cells to their correct position, the bioprinter robot needs a series of commands that must be obtained from the wound geometry; i.e., firstly, the wound's surface information (x and y) has to be extracted by segmentation; then, a 3D geometry is constructed using the depth information. Afterwards, the robot moves and dispenses cells on the 3D geometry guided by a series of commands.

To make printed patches biocompatible and usable for the human body, we need to carry skin cells inside a bio-compatible platform and place them on the surface of the wound. Thus, selecting and applying an appropriate biocompatible material for carrying and encapsulating cells is indispensable. Various methods exist, such as including cells in the bioprinter's gel-like ink to form a bio-ink. Hydrogels, which are applicable in bioprinting, can be classified into several groups according to their crosslinking methods. The process of crosslinking may be initiated by external triggers such as light [22], temperature [23], changes in environmental pH [24], presence of enzymes [25,26], or ionic cross-linkers [27]. Several review papers focusing on hydrogels in bioprinting provide readers with a rich source of further information in this regard [28-30].

Alginate is a polysaccharide derived from brown seaweeds and Alginate hydrogel has many interesting properties such as biocompatibility, low cost, and an easy gelation process making it a commonly used biopolymer for encapsulating cells. Due to its relatively high stiffness, any 3D scaffold fabricated with it has a good handling ability [31]. Despite the advantages of alginate hydrogel, the lack of cell binding sites causes weak interaction between the cells and the matrix, which eventually leads to limited cell proliferation [32].

The research questions for this study were: *Is it possible to obtain the 3D geometry, needed for 3D bioprinting of wounds using current image segmentation methods, and if so, which one is more robust and accurate?* The contribution of this work is to implement a calculated geometry for printing skin cells in a bio-compatible platform that aids in wound healing.

III. MATERIALS AND METHODS

The methodology is divided into two parts: image segmentation and bioprinting. For the former, it is adequate to capture images from a wound and upload them into the developed application. Using the provided graphical user interface, users would be able to choose the most-appropriate
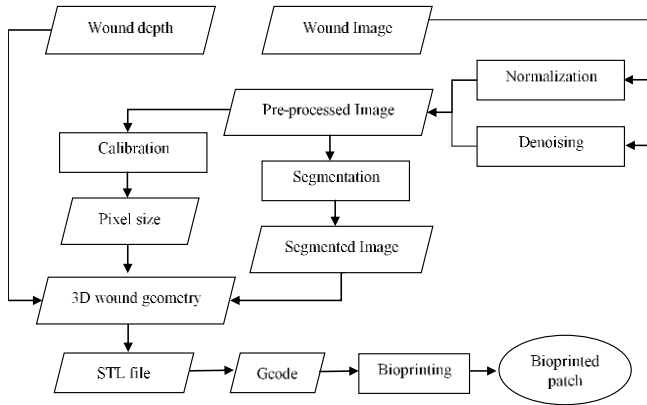
Fig. 2. Workflow diagram of the proposed study.

Diabetic, Granulation & Slough, F/63   Diabetic, Granulation, M/45

Metabolic, Necrosis, F/55   Burn, Granulation, M/17

Fig. 3. Samples of taken photos along with details of wound types and tissues, and patients gender/age.

segmentation method for each specific kind of wound. Then the wound geometry is accurately calculated, and via calibration to the actual values, the program provides the real area and boundaries of the wound. In the second step, the bioprinter robot, using appropriate materials, prints cells on the desired place. Fig. 2 presents a workflow diagram illustrating the overall pipeline of the proposed method.

A. Obtaining and preparing wound images

1) Acquiring wound images

While many image data bases are publically available, e.g., Dermquest Atlas [33] with more than 22,000 images, or the Brazilian Dermatology Atlas [34], the existing databases are not suitable for bioprinting for one or more of the following reasons: low resolution, lighting artefacts, and no appropriate indicators for wound dimensions. Therefore, in cooperation with the Wound and Ostomy Clinic of Erfan Hospital of Tehran, we collected a data set of chronic wounds, containing 26 photos of diabetic foot wounds, burns, and eschar. All of the photos were taken with a Canon 6D digital camera with a resolution of 5472 x 3648 (20 megapixels), and saved as RAW files, then down-sampled to 1368 x 912. While taking the photos, a ruler was placed beside and parallel to wound surfaces in order to obtain their precise scale and dimensions. Fig. 3 presents sample images, along with wound types and patient details. All of the results are reported based on the images of the Erfan data set.

2) Pre-processing of images

Image Intensity Normalization: For various reasons, e.g., glare, shadows, etc., the range of pixel intensity values may vary in different images. A linear normalization procedure is performed to eliminate these effects by applying the equation $N(i, j) = \frac{I(i, j) - G_{\min}}{G_{\max} - G_{\min}}$ to each color channel separately, where N is the normalized image, I is the grayscale intensity prior to normalization, and G_{max} and G_{min} are maximum and minimum intensity levels in the grayscale image respectively.

Denoising: The main filters used for image denoising is a Gaussian blurring filter with a standard deviation of σ = 0.5, shown to be very effective in removing camera noise for wound analysis [7]. However, in case there is a presence of salt and pepper noise (due to image capture), the operator is able to use the median filter.

B. Segmentation of wound in the 2D plane

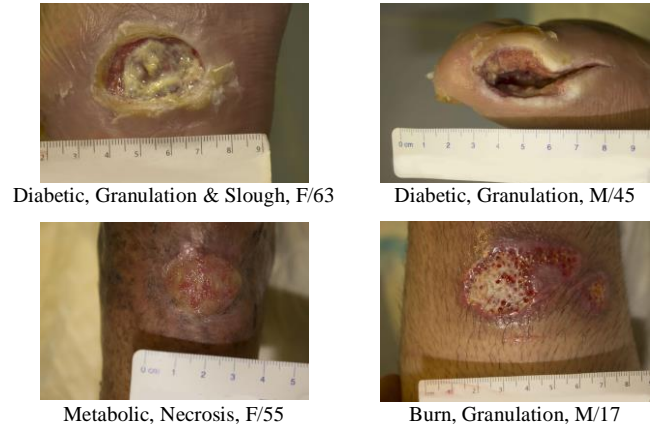Seven popular algorithms were implemented and applied to all images. Ground truth delineations were determined by a wound clinician who used an optical pen to draw the desired borders of wounds in the designed GUI.

1) Region-based methods

Region-growing [35]: Wound segmentation can be obtained based on the intensity similarity of wound pixels. First, a set of seed points P within the desired wounds is chosen by the clinician. Then for each k neighbors of q ($k = 4,8$), for the set of neighboring pixels available in P, if $|I_p - I_q| < M \pm 3\sigma$, (where M and σ are the mean value and the standard deviation of the selected pixel intensities), then point q is added to the set points P. Then this step is repeated for all pixels available in set P until no new point is added to this set and all pixels are dedicated to the desired wound region.

Active Contours without Edges (Chan-Vese (CV) model) [36]: This algorithm, unlike the classical Snake model, detects objects based on region similarities, not relying on gradients.

By assuming an evolving curve represented by ϕ as an initial level set function, and c_1 and c_2 as constant average intensities of inside and outside of ϕ in the image I, an energy function is defined as:

$$E(\phi, c_1, c_2) = \mu \int_{\Omega} \delta(\phi)|\nabla\phi|dx + \lambda_1 \int_{\Omega} H(\phi)|I - c_1|^2 dx + \lambda_2 \int_{\Omega} (1 - H(\phi))|I - c_2|^2 dx \quad (1)$$

in which $\mu=47$, $\lambda_1=\lambda_2=0.43$ are positive weighting parameters, chosen empirically, and $H(\phi)$ is a regularized Heaviside function. The first term ensures smooth boundaries, while the last two terms fit the level set to the image pixel data averaged over all RGB channels. The energy function is minimized using an iterative two-step algorithm in which c_1, c_2 are first computed while ϕ is considered fixed, then ϕ is updated [36].

2) Edge-based methods

Most chronic wounds have clear and distinguished boundaries, which make it possible to perform the segmentation based on the edges in the images. We compared three edge-based algorithms:

Edge and morphological operations: This method is based on the direct usage of image gradients. First, image gradients are obtained using a Sobel edge detector. Then, using morphological operations and structuring elements, e.g., diamond-shaped and linear, the obtained edges are dilated, unwanted margins are removed via thresholding, and the final image is eroded and smoothed [35].

Level set method preserving the distance function [37]: This algorithm is a level set method, which preserves the signed

distance function (SDF) that is necessary to accurately estimate geometric features and special curvatures of complex objects like wounds. The Lagrangian energy function is defined as:

$$E(\phi,\varphi,u,q,p,\Lambda) = \mu\int_{\Omega}\omega_b|q| + \lambda_1(\varphi-\phi) +$$
$$\frac{r_1}{2}(\varphi-\phi)^2 + \lambda_2(u-H(\varphi)) + \frac{r_2}{2}(u-H(\varphi))^2$$
$$+ \lambda_3(q-\nabla u) + \frac{r_3}{2}|q-\nabla u|^2 + \lambda_4(p-\nabla\phi) + \frac{r_4}{2}|p-\nabla\phi|^2 \quad (2)$$

in which ϕ is the SDF, φ is the non-linear term, $u = H(\varphi)$, $p = \nabla\varphi$, $q = \nabla u$, , ω_b is a boundary detection function, and $\Lambda = (\lambda_1,\lambda_2, \lambda_3, \lambda_4)$ are the Lagrangian functions. μ, the weight of edge term over the region term, was set to 0.3 empirically. An approximate solution is computed by iteratively alternating the minimization of the energy function with respect to each variable while considering the others fixed [37]. This method is sensitive to the size of the initial window and the images first need to be cropped.

Livewire: Some chronic wounds have outlier edges, e.g., detached skin, which do not determine the actual wound area and require supervision for a precise segmentation. The Livewire algorithm, also known as Intelligent Scissors [38], enables users to discard the outlier edges. In this method, first a seed point is chosen on a wound border. The objective is to determine a path from the seed to the mouse controlled pointer that follows the object boundaries. When the user moves the pointer, wound boundaries are extracted. The main local cost function is defined as [38]:

$$l(p,q) = \omega_Z.f_Z(q) + \omega_D.f_D(p,q) + \omega_G.f_G(q) \quad (3)$$

where f_Z, f_D and f_G are Laplacian zero-crossing, gradient direction and gradient magnitude cost terms, respectively, representing different aspects of edge features. The weights of the corresponding features were chosen empirically as follows: $\omega_Z=0.2$, $\omega_D=0.3$, $\omega_G=0.8$. The image edges were obtained using a Canny edge detector. The minimum cost function path was obtained using the Dijkstra algorithm [38].

Parametric active contour models- Snakes: A Snake is a deformable energy-minimizing curve with an energy functional as follows [39]:

$$E_{snake} = \int_0^1 E_{int}(v(s)) + E_{image}(v(s)) + E_{con}(v(s)) \quad (4)$$

$$E_{ext} = -|\nabla[G_\sigma(x,y)I(x,y)]|^2 \quad (5)$$

$$E_{int} = \frac{1}{2}[\alpha(s)|v_s(s)|^2 + \beta(s)|v_{ss}(s)|^2] \quad (6)$$

where α and β were set to 0.4 and 0.2 empirically. Edges were obtained on the grayscale intensity image. The clinician initializes the Snake contour and using (4) the contour evolves to match image features. The Viterbi algorithm was used for optimization [40].

3) *Texture-based methods*

Houhou-Thiran-Bresson model (HTB): Wound tissue images usually have specific textures, which is a prominent feature to distinguish between wound region and other parts of the image and extract the wound geometry. An intrinsic texture descriptor, which describes the geometry of textures using semi-local image information and tools from differential geometry [41], is defined as: $F = \exp\left(-\frac{\det(g_{xy})}{\sigma^2}\right)$, in which g_{xy} is the corresponding metric tensor and $\sigma > 0$ is a scaling parameter. Using the Kullback-Leibler (KL) distance between
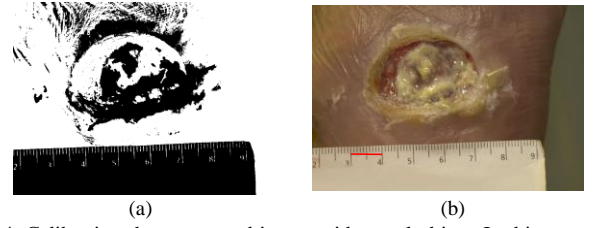

Fig. 4. Calibrating the segmented image with a real object. In this example, per cm equals 492.2 pixels in the image. Thus, each pixel is 412.78 μm². The length of the wound is 3.246 cm (1598.07 pixels), its width is 1.811 cm (891.09 pixels) and the area is 1280919 pixels which equals 5.2874 cm². (a) binarized image in red channel (b) primary image with detected ruler and obtained scale.

probability distribution function (pdf), an active contour model which distinguishes the background and desired textures can be designed by minimizing the following energy function:

$$E = \int_{R+}\left(q_{in}(F,\Omega)\log\frac{q_{in}(F,\Omega)}{q_{out}(F,\Omega)} + q_{out}(F,\Omega)\log(\frac{q_{out}(F,\Omega)}{q_{in}(F,\Omega)})\right) + \lambda\underbrace{\int_{\partial\Omega}ds}_{L(\Omega)} \quad (7)$$

where q_{in}, q_{out} are the inside and outside pdfs respectively, Ω is the evolving region, and $\lambda=1.75$ is the coefficient for regularizing the evolving curve which was chosen empirically. The first term belongs to the KL distance and the second term is a curvature regularization term. Finally, the Split-Bregman method [42] was used for optimization.

C. *Segmentation evaluation*

Statistical significances: Student's t-test was performed on each pair of segmentation algorithms under the null hypothesis that the accuracy of each pair of the implemented segmentation methods is the same. The tests were carried out at the significance level of 0.05.

Performance and correctness measures of segmentation: By intersecting a segmented image with the corresponding ground truth, four outcome relative states, i.e., True Positive, False Positive, True Negative, False Negative, were obtained, based on which the four validation indicators of Precision, Sensitivity, Specificity, and Accuracy were defined. In addition, the Jaccard index (JI) [43], Dice similarity coefficient (DS) [44] and Hausdorff Distance (HD) [45] were used to evaluate the performance of the segmentation.

D. *Calibrating the segmented image with a real object*

In order to scale a segmented image to real object size, a ruler sticker [8] is placed on the imaging plane and parallel to the surface of the wounds as the size reference with the camera held perpendicular to the wound surface. To calibrate the physical dimensions of pixels, an automated procedure is used: First, unnecessary image details and wound are removed via thresholding, to keep the ruler lines. Then the remaining blobs in the image are labeled, sorted and categorized. Finally, by finding the distance between the largest blobs in the image, the number of pixels per centimeter is obtained, from which the obtained coordinates and area are calibrated. Fig. 4 presents the calibratrion procedure for a sample wound image.

E. *Setting the depth of the 3D coordinates for 3D printing*

The segmented regions provide wound coordinates on a 2D plane. However, 3D bioprinting requires 3D wound coordinates (length, width, and depth). For the current proof-of-concept stage of this study, i.e., for evaluating different bioprinting parts, such as the bio-ink features, e.g., elasticity,

TABLE II.
RESULTS OF THE SEGMENTATION EVALUATION INDICATORS TESTS. THE VALUES ARE AVERAGE OF ALL MEASURES ACROSS THE DATA SET.

| Algorithm	Precision	Accuracy	Sensitivity	Specificity	Jaccard Index	Dice Similarity	Hausdorff Distance	Variance
Edge detection	84.53	88.14	99.96	89.75	89.14	94.26	46.63	32.12
Region growing	83.49	89.22	**100**	87.67	87.63	93.38	52.04	28.65
Livewire	97.44	**97.08**	99.83	**96.67**	**96.22**	**98.15**	**32.26**	8.65
Snakes	92.12	93.74	99.68	92.47	88.21	93.74	56.65	**6.24**
LS	**98.77**	94.54	99.71	92.89	88.93	94.14	54.66	10.37
HTB model	97.42	87.50	98.37	86.93	71.84	83.61	132.23	28.11
CV Model	98.44	95.26	98.95	87.41	70.72	82.85	127.78	34.19
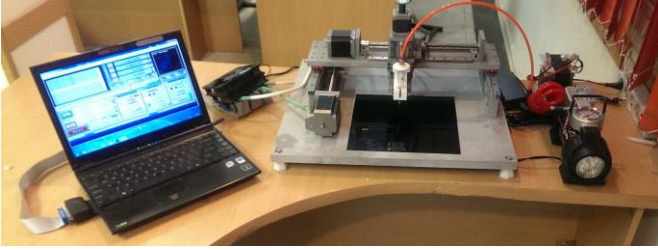
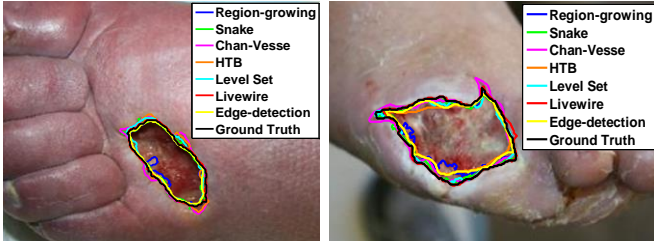Fig. 5. The bioprinter robot in the Biomedical Engineering department of Amirkabir University.

Fig. 6. Segmentation results of different methods and ground truth. The blue, green, red, yellow, black colors correspond to region growing, edge detection, snake, livewire, ground truth results respectively.

accuracy, and the performance of the bio-printer and the efficacy of the segmentation algorithms, the wound depth was considered uniform. The uniform values were set based on an approximation, performed by a clinician using the most common clinical wound depth measuring method [46]: the cotton-tipped applicator is placed into the deepest area of the wound and a mark is also placed on the applicator at the skin level. The applicator is then held against a metric ruler to measure the wound depth [46, 47]. If the depth varies, the measurements are taken in different areas. The recorded depth will be the deepest area of the wound measured [47].

F. Converting the obtained coordinates to the numerical control programming language

Obtained coordinates should be converted into numerical control programming language to let the bioprinter move on the specified paths and print the desired pattern. Currently, the bioprinter robot in the Biomedical Engineering Department of Amirkabir University (Fig. 5) works on *mach3* [48] control software and requires G-code motor codes to move and dispense cells. G-code is the general name for numerical control programming, which is widely used in 3D printing and controls how instruments, other accessories, and machine equipment move.

Most G-code generator programs need *STL* (STereoLithography) file format. To save the obtained geometries into STL files, the open source MATLAB code in [49] was used with no modifications. Fig. 7(c) presents the 3D

form of a simulated STL file. G-codes were generated from the simulated STL files using the *MankatiUM 6.5.3* software [50].

G. Bio-printing materials and synthesis

Sodium-alginate (Alginic acid sodium salt from brown algae), calcium-chloride di-hydrated and gelatin from bovine skin were obtained from sigma-Aldrich. To handle the weak interaction between the cells and the matrix and limited cell proliferation, we added some gelatin to the composition of our bio-ink. Gelatin is obtained by partial hydrolysis of the triple helix structure of collagen into single-strain molecules [51]. Therefore, gelatin is the most similar biopolymer to collagen, which could mimic the extra cellular matrix and enhance the cell adhesion properties of the structure at a low cost.

Alginate-gelatin hydrogel was synthesized by dissolving 16% (w/v) sodium-alginate and 4% (w/v) gelatin in deionized water. High viscosity of hydrogel was considered for a better resolution and an optimized cell viability.

We printed the described geometries in a dish utilizing bio-ink hydrogel, which consisted of alginate and gelatin. For a better adhesion of the first layer to the dish, it was washed by di-ionized water and dried with pressurized air. Sodium-Alginate blend with gelatin was printed using a pneumatic dispensing nozzle. Ionic gelation took place by soaking the bio-printed gel in 4% (w/v) calcium-chloride solution for 5 min after the process. Crosslinking density was adjusted in order to preserve the printed gel geometry within the shortest time possible. Then, the dish was filled with deionized water to keep the sample from dehydrating.

IV. RESULTS

A. Experimental setup

The bioprinting experimental setup consisted of a custom-made bioprinter, a hydrogel dispensing module, and a PC controlled software. The bioprinter machine itself consisted of a 3-axis motion control stage with a hydrogel injection module mounted on its head. Using the PC controlled software, the tool path was translated to XYZ coordinates, guiding the motor drivers to move along the 3-axes. The dispensing module was composed of a filled syringe and a pump connected through a sealed tube. The deposition rate of alginate-gelatin viscose solution was controlled by setting a steady air pressure behind the hydrogel. The addition of Calcium-chloride for ionic-gelation was performed manually using a 5 ml syringe.

B. Segmentation evaluation

Performance and correctness measures of segmentation: Fig. 6 represents the performance of different image segmentation methods on two sample images. Segmentation evaluation results are summarized in Table II: Livewire resulted in the highest accuracy. Furthermore, all methods were sensitive enough, and therefore, had a low type II error. The

<div style="text-align:center">(a)   (b)   (c)   (d)   (e)   (f)</div>
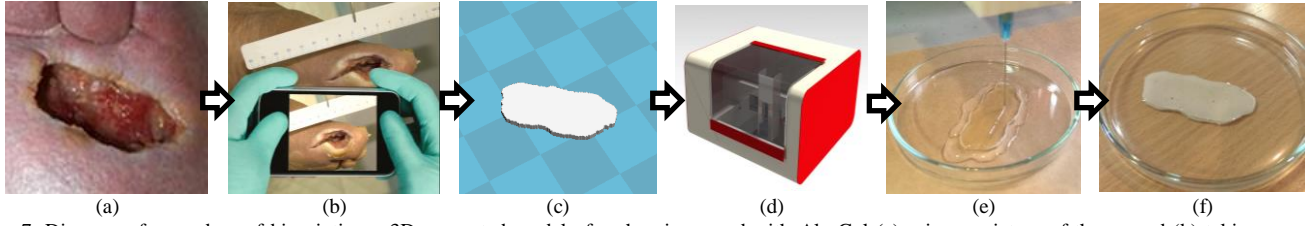
Fig. 7. Diagram of procedure of bioprinting a 3D generated model of a chronic wound with Alg-Gel (a) primary picture of the wound (b) taking wound photos and using a ruler indicator and performing image segmentation (c) simulated 3D model (d) inserting STL file into the bioprinter robot (e) printed patch while printing. The transparent liquid surrounding gel is calcium-chloride which has not reacted with alginate-gelatin yet. (f) Reacted and hard-set Alg-Gel after injecting calcium-chloride.

results also illustrated that Livewire with specificity of 96.67% had the lowest type I error rate. Furthermore, other metrics, i.e., JI, DS, and HD were significantly higher for Livewire, indicating that it had the best performance.

Computation cost and user interaction: Table III presents average elapsed time and user interaction. It is not straightforward to evaluate these measures since different implementations of the same method may reduce user-interaction (e.g., auto-initialization) at the expense of lower accuracy. What we report is our experience with the aforementioned segmentation methods. The Snakes is the most time consuming method as it must be carefully initialized to avoid getting stuck in erroneous local minima. On the other hand, the interactive Livewire demands less computation (given its efficient dynamic programming optimization) but needs more user interaction to ensure the proper delineation compared to the other methods. For bioprinting, with respect to the tradeoff between computational complexity and accuracy, the latter is more important and Livewire's higher accuracy outweighs the required user interaction.

Statistical significances: The results of the t-tests for all of the paired implemented algorithms returns $p<0.05$ and $h=1$, while h is the hypothesis test result, returned as a logical value. This indicates the rejection of the null hypothesis at the significance level which is 0.05. The null hypothesis for the t-test was that the evaluation indicators of all of the implemented segmentation methods are the same.

C. Bioprinting results

The bioprinter robot is able to print skin cells on skin surface from validated G-codes. In this study, the average obtained pixel size after calibration is about 20 μm. Fig. 7(f) and 7(e) illustrate sample results. A clinician, using a scaled ruler, measured the actual wound dimensions, i.e., width and height, for further evaluation of similarity between the bioprinted patches and the corresponding wounds. Comparing the measurements of width and height for two bioprinted patch instances with the actual corresponding wound dimensions demonstrated an average similarity of 95.56% between the two.

V. DISCUSSION

The objective of this study was to provide proof-of-concept for a segmentation and bioprinting tool to facilitate chronic wound treatment. The semi-automatic segmentation enables users to extract wound boundaries from images using prior knowledge about wounds and bioprinting. The average performance values for the Livewire, are relatively higher than most of the previous works in Table I, indicating that the proposed method, despite all current limitations, would be an appropriate selection for this application.

TABLE III.
COMPUTATION COST AND USER INTERACTION OF THE IMPLEMENTED SEGMENTATION METHODS. THE REPORTED NUMBERS FOR m AND σ IN THE TABLE ARE THE AVERAGE VALUES OF MEAN AND VARIANCE OVER ALL IMAGES RESPECTIVELY.

Algorithm	Total time (sec)		Computation Time (sec)		User Interaction (Mouse Clicks)	
	m	σ	m	σ	m	σ
Edge detection	5.02	0.85	1.03	0.001	1	0.17
Region growing	11.34	0.48	3.47	0.01	2	0.60
Livewire	17.80	5.91	2.19	0.007	4	1.62
Snakes	28.55	11.38	10.99	0.01	10	5.32
LS (170 iterations)	23.64	0.51	22.49	0.003	0	0
CV model	2.12	0.26	0.59	0.001	1	0.14
HTB model	3.01	0.33	1.18	0.009	1	0.19

Typically, human cells have a dimension of 20-30 μm [52]. Since the bioprinter robot does not use a single cell delivery technique, it moves with a precision of 100 μm, meaning that it is able to move to a location with a precision of 100 μm and dispense the bio-ink. Therefore, segmentation results must have at least a precision of 100 μm. Coarser segmentation and depth resolution would result in coarser coordinates for the STL model and 3D geometry, and consequently, the bioprinter would not be able to move and dispense over all of the wound area, especially if it has more complexity and detailed edges. In this study, the average obtained pixel size after calibration is about 20 μm, indicating that the proposed method is capable of distinguishing between each 20 μm on a wound surface. This value properly fulfills the bioprinter requirements and confirms the proposed method's capability to print accurate patches.

Based on Table III, both Livewire and Snakes need a higher level of interaction than the other methods. In addition, using user-guided external forces, the Snakes algorithm is able to obtain a higher accuracy at the expense of increased user interaction, which we found to be too cumbersome and time-consuming for users. Thus, the Livewire is able to obtain the desired level of accuracy with less user interaction. Future work could involve automatic segmentation methods which are insensitive to initialization and have energy cost terms derived from large scale training of machine learning algorithms.

This study did not include color calibration, as the proposed segmentation methods do not use color information to determine size and wound geometry. In future studies, tissue classification can fulfill the need for determining the different tissues and preparing different cells for real bioprinting in the various layers of skin. By calibrating colors and using color and texture descriptors [10-12] or a Red-Yellow-Black-White (RYKW) map [6], wound tissues can be classified.

All the segmentation methods have been applied by the same person and compared to a single ground truth. Recruiting

more than one user to perform the segmentation and more than one expert clinician to determine the ground truth is a possibility for future work, and will allow us to assess inter-user variability and agreement across clinicians [6].

Although the data set used in this study justifies the performance of the proposed bioprinting pipeline, a thorough understanding of the proposed method's performance on wounds of different shapes and types, and of the effect of wound geometry on the bioprinting results calls for additional studies on larger data sets.

The ruler method used for calibration, while providing the physical dimensions of pixels on flat surfaces, is not able to consider the curvature of an imaged wound. Therefore, the actual dimensions for wounds on convex surfaces would be slightly different. Thus, instead of using a ruler and controlling the imaging conditions, a color checkerboard and a calibration algorithm, e.g., Direct Linear Transformation [53], can be used to obtain a camera matrix and study the effects of intrinsic and extrinsic camera parameters as well as wound curvature on bioprinting results.

Although the primary measurements results of the overlap between the bioprinted patch and the corresponding wound dimensions indicate a good match, a moulage phantom can be used to further assess the overlap between the bioprinting result and the wound imposed on the phantom. Also, the comparison can be performed based on a pixel-by-pixel method by capturing an image of the bioprinted patch and matching each pixel to the corresponding pixel on the wound image.

Before placing a bioprinted patch on skin, it is important to completely prepare the wound bed during a procedure called debridement. Any necrotic tissue or foreign material must be removed from areas around the wound in order to increase the chances of healing. Similarly, especially before image segmentation, debridement of the wound area is important because the open wound bed cannot be observed and assessed effectively in the presence of necrotic tissue [54].

The current preliminary stage of this study was retrospective, in which only mono (not stereo) sets of images were available. Hence, wound depth was not available but rather was considered uniform, which poses a certain limitation on the proposed method. The bio-ink, due to its characteristics and deformability, can completely fill the wound volume. However, it is expected that a strategy be deployed in future research to precisely obtain the third dimension of wounds. The most common method uses a description of the tissues involved as opposed to an actual measurement [55]. Another method uses 3D reconstruction from stereo images. Applying structures from motion (SFM) algorithms can obtain dense estimation of the surface geometry from two widely separated views. Due to several wound image characteristics, e.g., the uniform texture, small scale and baseline, etc., this SFM method confronts some challenges in finding the correspondence and ensuring proper image matching. Although these challenges can be partially tackled by incorporating wound specific shape priors, extracted from pre-operative images [56], this method is expensive, needs special equipment (synchronization of two cameras, keeping the patient still, etc.), and requires a robust image processing chain [57]. Another alternative involves replacing depth values simply with the ones obtained from a laser depth-detecting sensor [52], which is more accurate and has a lower computational cost, but is more expensive.

VI. CONCLUSION

We presented a novel approach for healing chronic wounds. The semi-automatic image segmentation method gives clinicians much higher control by providing more-efficient coordinates for bioprinting. Based on the results of Table II, the Livewire algorithm is the most efficient of those tested, with 97.08%, 99.68%, and 96.67%, 96.22, 98.15, and 32.26, respectively, in terms of accuracy, sensitivity, specificity, Jaccard Index, Dice Similarity Coefficient and Hausdorff Distance respectively.

We used completely biocompatible materials in providing cell printing platforms. Alginate-gelatin hydrogel was synthesized by dissolving 16% (w/v) sodium-alginate and 4% (w/v) gelatin in deionized water and, due to its desirable properties such as biocompatibility, low cost and an easy gelation process, was used as the biopolymer for cell encapsulation.

The bioprinting results demonstrate 95.56% similarity between the bioprinted patch dimensions and the desired wound geometries, which represents a good match and overlap.

In future works, we plan to classify different wound tissues, use a more-comprehensive data set, and improve the validation and calibration techniques to obtain more precise and reliable coordinates for bioprinting. Furthermore, we plan to design a precise method for estimating the wound's depth.

ACKNOWLEDGMENT

REFERENCES

[1] K. Jung, S. Covington, C. Sen, M. Januszyk, R. Kirsner, G. Gurtner and N. Shah, "Rapid identification of slow healing wounds", *Wound Rep and Reg*, vol. 24, no. 1, pp. 181-188, 2016.

[2] A. Dababneh and I. Ozbolat, "Bioprinting Technology: A Current State-of-the-Art Review", *J. of Manufacturing Science and Eng.*, vol. 136, no. 6, pp. 061016, 2014.

[3] M. Bilgin and Ü. Güneş, "A Comparison of 3 Wound Measurement Techniques", *J. of Wound, Ostomy and Continence Nursing*, vol. 40, no. 6, pp. 590-593, 2013.

[4] A. Shah, C. Wollak and J. Shah, "Wound Measurement Techniques: Comparing the Use of Ruler Method, 2D Imaging and 3D Scanner", *J. of the American College of Clinical Wound Specialists*, vol. 5, no. 3, pp. 52-57, 2013.

[5] J. Thatcher, J. Squiers, S. Kanick, D. King, Y. Lu, Y. Wang, R. Mohan, E. Sellke and J. DiMaio, "Imaging Techniques for Clinical Burn Assessment with a Focus on Multispectral Imaging", *Advances in Wound Care*, 2016.

[6] M. Fauzi, I. Khansa, K. Catignani, G. Gordillo, C. Sen and M. Gurcan, "Computerized segmentation and measurement of chronic wound images", *Comput. in Biology and Medicine*, vol. 60, pp. 74-85, 2015.

[7] L. Wang, P. Pedersen, D. Strong, B. Tulu, E. Agu and R. Ignotz, "Smartphone-Based Wound Assessment System for Patients With Diabetes", *IEEE Trans. Biomed. Eng.*, vol. 62, no. 2, pp. 477-488, 2015.

[8] C. Loizou, T. Kasparis and M. Polyviou, "Evaluation of wound healing process based on texture image analysis", *J. of Biomed. Graph. and Computing*, vol. 3, no. 3, 2013.

[9] C.P. Loizou, T. Kasparis, O. Mitsi, M. Polyviou, "Evaluation of wound healing process based on texture analysis", in *Proc. IEEE Int. Conf. Bioinf. Bioeng.*, pp. 709–714, 2012.

[10] H. Wannous, S. Treuillet, Y. Lucas, "Supervised tissue classification from color images for a complete wound assessment tool," in *Proc. IEEE EMBS Int. Conf.*, pp. 6031–6034, 2007.

[11] H. Wannous, Y. Lucas, S. Treuillet, and B. Albouy, "A complete 3D wound assessment tool for accurate tissue classification and measurement," in *Proc. IEEE 15th Conf. Image Process.*, pp. 2928–2931, Oct. 2008.

[12] H. Wannous, Y. Lucas and S. Treuillet, "Enhanced Assessment of the Wound-Healing Process by Accurate Multiview Tissue Classification," *IEEE Trans. Med. Imag.*, vol. 30, no. 2, pp. 315-326, 2011.

[13] N.D.J. Hettiarachchi, R.B.H. Mahindaratne, G.D.C. Mendis, H.T. Nanayakkara, N.D. Nanayakkara, "Mobile-based wound measurement," in *Proc. IEEE Point-of-Care Healthcare Technol.*, pp. 298–301, 2013.

[14] F. Veredas, H. Mesa, L. Morente, "Binary tissue classification on wound images with neural networks and bayesian classifiers," *IEEE Trans. Med. Imag..*, vol. 29, no. 2, pp. 410–427, 2010.

[15] A.F.M. Hani, L. Arshad, A.S. Malik, A. Jamil, F. Yap, "Haemoglobin distribution in ulcers for healing assessment," in *Proc. Int. Conf. on Intelligent and Advanced Syst.*pp. 362–367, 2012.

[16] A.A. Perez, A. Gonzaga, J.M. Alves, "Segmentation and analysis of leg ulcers color images", in *Proc. Int. Workshop Med. Imaging and Augmented Reality*, pp. 262–266, 2001.

[17] K. Wantanajittikul, N. Theera-Umpon, S. Auephanwiriyakul, T. Koanantakool, "Automatic segmentation and degree identification in burn color images," in *Proc. Int. Conf. Biomed. Eng.*, pp. 169–173, 2011.

[18] B. Song, A. Sacan, "Automated wound identification system based on image segmentation and artificial neural networks", in *Proc. IEEE Int. Conf. Bioinformatics and Biomedicine*, pp. 1–4, 2012.

[19] M. Kolesnik, A. Fexa, "Segmentation of wounds in the combined color-texture feature space", in *Proc. SPIE Med. Imaging*, vol. 5370, pp. 549–556, 2004.

[20] M. Kolesnik, A. Fexa, "How robust is the SVM wound segmentation?", in *Proc. NORDIC Signal Process. Symp.*, pp. 50–53, 2006.

[21] M. Silveira, J. Nascimento, J. Marques, A. Marcal, T. Mendonca, S. Yamauchi, J. Maeda and J. Rozeira, "Comparison of Segmentation Methods for Melanoma Diagnosis in Dermoscopy Images*", IEEE J. Sel. Top. Signal Process.*, vol. 3, no. 1, pp. 35-45, 2009.

[22] A. Skardal, J. Zhang, L. McCoard, X. Xu, S. Oottamasathien and G. Prestwich, "Photocrosslinkable Hyaluronan-Gelatin Hydrogels for Two-Step Bioprinting", *Tissue Eng. Part A*, vol. 16, no. 8, pp. 2675-2685, 2010.

[23] S. Chen, Y. Wu, F. Mi, Y. Lin, L. Yu and H. Sung, "A novel pH-sensitive hydrogel composed of N,O-carboxymethyl chitosan and alginate cross-linked by genipin for protein drug delivery", *J. of Controlled Release*, vol. 96, no. 2, pp. 285-300, 2004.

[24] Jin, R., Hiemstra, C., Zhong, Z., & Feijen, J., "Enzyme-mediated fast in situ formation of hydrogels from dextran–tyramine conjugates," *Biomaterials*, vol. 28, no. 18, pp. 2791–2800, 2007.

[25] S. Sershen, S. Westcott, N. Halas and J. West, "Temperature-sensitive polymer-nanoshell composites for photothermally modulated drug delivery", *J. Biomed. Materials Res.*, vol. 51, no. 3, pp. 293-298, 2000.

[26] Z. Yang, H. Gu, D. Fu, P. Gao, J. Lam and B. Xu, "Enzymatic Formation of Supramolecular Hydrogels", *Adv. Mater.*, vol. 16, no. 16, pp. 1440-1444, 2004.

[27] C. Kuo and P. Ma, "Ionically crosslinked alginate hydrogels as scaffolds for tissue engineering: Part 1. Structure, gelation rate and mechanical properties", *Biomaterials*, vol. 22, no. 6, pp. 511-521, 2001.

[28] D. Kirchmajer, R. Gorkin III and M. in het Panhuis, "An overview of the suitability of hydrogel-forming polymers for extrusion-based 3D-printing", *J. Mater. Chem. B*, vol. 3, no. 20, pp. 4105-4117, 2015.

[29] J. Malda *et al.,* "25th Anniversary Article: Engineering Hydrogels for Biofabrication", *Adv. Mater.*, vol. 25, no. 36, pp. 5011-5028, 2013.

[30] S. Wang, J. Lee and W. Yeong, "Smart hydrogels for 3D bioprinting", *Int. J. Bioprinting*, 2015.

[31] A. Augst, H. Kong and D. Mooney, "Alginate Hydrogels as Biomaterials", *Macromol. Biosci.*, vol. 6, no. 8, pp. 623-633, 2006.

[32] J. Rowley, G. Madlambayan and D. Mooney, "Alginate hydrogels as synthetic extracellular matrix materials", *Biomaterials*, vol. 20, no. 1, pp. 45-53, 1999.

[33] Dermquest.com, "DermQuest: Home", 2015, [Online], Available: http://www.dermquest.com/ [Accessed: 06- Nov- 2015].

[34] Atlasdermatologico.com.br, "Dermatology Atlas", 2016, [Online]. Available: http://www.atlasdermatologico.com.br, [Accessed: 12- Nov-2015].

[35] R. C. Gonzalez and R. E. Woods, *Digital image processing*, 3rd ed. Reading, Massachusetts: Addison-Wesley Publishing Company, 2007.

[36] T. Chan and L. Vese, "Active contours without edges", *IEEE Trans. Image Process*, vol. 10, no. 2, pp. 266-277, 2001.

[37] V. Estellers, D. Zosso, Rongjie Lai, S. Osher, J. Thiran and X. Bresson, "Efficient Algorithm for Level Set Method Preserving Distance Function", *IEEE Trans. Image Process.*, vol. 21, no. 12, pp. 4722-4734, 2012.

[38] E. N. Mortensen and W. A. Barrett, "Intelligent scissors for image composition," in *SIGGRAPH '95 Proc. 22nd annu. conf. on Comput. Graph. and interactive techniques,* pp. 191-198, 1995.

[39] M. Kass, A. Witkin and D. Terzopoulos, "Snakes: Active contour models", *Int. J. Comput. Vision*, vol. 1, no. 4, pp. 321-331, 1988.

[40] A. Amini, T. Weymouth and R. Jain, "Using dynamic programming for solving variational problems in vision", *IEEE Trans. Pattern Anal. Mach. Intell.*, vol. 12, no. 9, pp. 855-867, 1990.

[41] Houhou, Nawal, Jean-Philippe Thiran, and Xavier Bresson. "Fast texture segmentation based on semi-local region descriptor and active contour."*Numerical Mathematics: Theory, Methods and Applications.* pp. 445-468, 2009.

[42] T. Goldstein, X. Bresson, and S. Osher, "Geometric Applications of the Split Bregman Method: Segmentation and Surface Reconstruction", *Journal of Scientific Computing*, 45(1-3), pp. 272-293, 2010

[43] P. Jaccard, "The distribution of the flora in the alpine zone", *New Phytologist.* vol. 11, no. 2, pp. 37-50, 1912.

[44] L. Dice, "Measures of the Amount of Ecologic Association Between Species", Ecology, vol. 26, no. 3, pp. 297-302, 1945.

[45] D. Huttenlocher, G. Klanderman and W. Rucklidge, "Comparing images using the Hausdorff distance", *IEEE Trans. Pattern Anal. Mach. Intell.,* vol. 15, no. 9, pp. 850-863, 1993.

[46] Bryant, R. and Nix, D., *Acute and chronic wounds*, 5th ed., Elsevier Health Sciences, 2015.

[47] Wound Care Education Institute, N. Morgan, *Skin and wound resource manual,* Wound Care Education Institute; 2006.

[48] Mach3 version 3.043.062, Livermore Falls: ArtSoft USA, 2012.

[49] Sven, 2015. *stlwrite - Write binary or ascii STL file,* [Online] Available at: http://www.mathworks.com/

[50] MankatiUM version 6.5.3 Shanghai: Mankati, 2015.

[51] X. Shu, Y. Liu, F. Palumbo and G. Prestwich, "Disulfide-crosslinked hyaluronan-gelatin hydrogel films: a covalent mimic of the extracellular matrix for in vitro cell growth", *Biomaterials*, vol. 24, no. 21, pp. 3825-3834, 2003.

[52] K. W. Binder , "In situ bioprinting of the skin" , *Ph.D. dissertation in molecular genetics and genomics* , 2011.

[53] H. Hatze, "High-precision three-dimensional photogrammetric calibration and object space reconstruction using a modified DLT-approach." *J. of biomechanics,* vol. 21, no. 7, pp. 533-538, 1988.

[54] J. S. Boateng, K. H. Matthews, H. N. Stevens, G. M. Eccleston, "Wound healing dressings and drug delivery systems: a review" *J. of pharmaceutical sciences*, vol. 97, no. 8, pp. 2892-2923, 2008.

[55] B. Yates, *Merriman's assessment of the lower limb*. Edinburgh: Churchill livingstone, 2012, p. 508.

[56] A. Amir-Khalili, J. M. G.Peyrat, G. Hamarneh, R. Abugharbieh, "3D surface reconstruction of organs using patient-specific shape priors in robot-assisted laparoscopic surgery." *Abdominal Imaging. Computation and Clinical Applications*., pp. 184-193, 2013.

[57] S. Treuillet, B. Albouy, and Y. Lucas, "Three-dimensional assessment of skin wounds using a standard digital camera," *IEEE Trans. Med.Imag.*, vol. 28, pp. 752–762, May 2009.